

# The evolution of white dwarfs resulting from helium-enhanced, low-metallicity progenitor stars.

Leandro G. Althaus<sup>1,2</sup>, Francisco C. De Gerónimo<sup>1,2</sup>, Alejandro H. Córscico<sup>1,2</sup>, Santiago Torres<sup>3,4</sup>, and Enrique García-Berro<sup>3,4</sup>

<sup>1</sup> Grupo de Evolución Estelar y Pulsaciones. Facultad de Ciencias Astronómicas y Geofísicas, Universidad Nacional de La Plata, Paseo del Bosque s/n, 1900 La Plata, Argentina

<sup>2</sup> IALP - CONICET

<sup>3</sup> Departament de Física, Universitat Politècnica de Catalunya, c/Estève Terrades 5, 08860 Castelldefels, Spain

<sup>4</sup> Institute for Space Studies of Catalonia, c/Gran Capita 2-4, Edif. Nexus 201, 08034 Barcelona, Spain

Received ; accepted

## ABSTRACT

**Context.** Some globular clusters host multiple stellar populations with different chemical abundance patterns. This is particularly true for  $\omega$  Centauri, which shows clear evidence of a helium-enriched sub-population characterized by a helium abundance as high as  $Y = 0.4$

**Aims.** We present a whole and consistent set of evolutionary tracks from the ZAMS to the white dwarf stage appropriate for the study of the formation and evolution of white dwarfs resulting from the evolution of helium-rich progenitors.

**Methods.** White dwarf sequences have been derived from progenitors with stellar mass ranging from 0.60 to 2.0  $M_{\odot}$  and for an initial helium abundance of  $Y = 0.4$ . Two values of metallicity have been adopted:  $Z = 0.001$  and  $Z = 0.0005$ .

**Results.** Different issues of the white dwarf evolution and their helium-rich progenitors have been explored. In particular, the final mass of the remnants, the role of overshooting during the thermally-pulsing phase, and the cooling of the resulting white dwarfs differ markedly from the evolutionary predictions of progenitor stars with standard initial helium abundance. Finally, the pulsational properties of the resulting white dwarfs are also explored.

**Conclusions.** We find that, for the range of initial masses explored in this paper, the final mass of the helium-rich progenitors is markedly larger than the final mass expected from progenitors with the usual helium abundance. We also find that progenitors with initial mass smaller than  $M_{\star} \approx 0.65 M_{\odot}$  evolve directly into helium-core white dwarfs in less than 14 Gyr, and that for larger progenitor masses the evolution of the resulting low-mass carbon-oxygen white dwarfs is dominated by residual nuclear burning. For helium-core white dwarfs, we find that they evolve markedly faster than their counterparts coming from standard progenitors. Also, in contrast with what occurs for white dwarfs resulting from progenitors with the standard helium abundance, the impact of residual burning on the cooling time of white dwarfs is not affected by the occurrence of overshooting during the thermally-pulsing phase of progenitor stars.

**Key words.** stars: evolution — stars: interiors — stars: white dwarfs

## 1. Introduction

It is now well established that a handful of globular clusters harbour multiple stellar populations characterized by different He enrichments (Bastian et al. 2015). This is the case for instance for  $\omega$  Centauri (Norris 2004; Joo & Lee 2013; Tailo et al. 2016), NGC 2808 (D’Antona et al. 2005; Milone et al. 2012), and NGC 6441 (Caloi & D’Antona 2007; Bellini et al. 2013b) in which sub-populations are clearly visible in their respective color-magnitude diagrams. In particular, He enrichments as high as  $Y \sim 0.4$  have been suggested to explain the observed split main sequences and Horizontal Branches (HB) of  $\omega$  Centauri and NGC 2808. Because an increase in He abundance decreases the turnoff mass of a stellar population, the presence of a He-enriched sub-population has also been invoked to account for the presence of hot and extreme HB stars (D’Antona & Caloi 2008), as well as the existence of a large fraction of He-core white dwarfs in some globular clusters, like  $\omega$  Centauri (Calamida et al. 2008; Bellini et al. 2013a). The origin of these He-rich sub-populations is believed to result from cluster self-pollution caused by the ejecta of massive-

intermediate mass Asymptotic Giant Branch (AGB) stars of the first generation after the occurrence of the second dredge-up and hot bottom burning stage (Ventura et al. 2001), from fast rotating massive stars (Decressin et al. 2007), or from evolved Red Giant Branch (RGB) stars that experienced extra-deep mixing (Denissenkov & Weiss 2004) — see also Bastian et al. (2015) for a recent discussion about this issue.

The detection of white dwarf cooling sequences of globular clusters is specially interesting, since it allows studying fundamental properties of these stars and of the corresponding stellar populations. Because of their well understood evolutionary properties (Fontaine & Brassard 2008; Winget & Kepler 2008; Althaus et al. 2010b), white dwarfs can be used as distance indicators and as independent reliable cosmic clocks to date a wide variety of stellar populations, such as our Galaxy — see García-Berro & Oswalt (2016), and references therein, for a recent review on this topic — and open and globular clusters — see Winget et al. (2009), García-Berro et al. (2010), Jeffery et al. (2011), Bono et al. (2013) and Hansen et al. (2013) for some examples.

Recently, Althaus et al. (2015) have explored the evolution of white dwarfs formed in metal-poor populations, and found that stable hydrogen burning dominates their cooling even at low luminosities. They found that the role played by such residual burning is independent of the rate at which stellar mass is lost during the AGB and post-AGB evolution of progenitors, but depends on the occurrence of overshooting during the thermally-pulsing (TP) AGB phase. In particular, overshooting results in a carbon enrichment of the envelope due to third dredge-up episodes. Carbon enrichment eventually results in final thinner hydrogen envelopes, which are unable to sustain appreciable hydrogen burning during the white dwarf stage. Here, we extend the scope of the study of Althaus et al. (2015) to explore the impact of an initial He-enrichment on the formation, evolution and pulsational properties of the resulting white dwarf stars.

Our main aim is to provide a consistent set of evolutionary tracks from the ZAMS to the cooling phase appropriate for the study of white dwarfs with helium and carbon-oxygen cores formed in He-rich sub-populations. The white dwarf evolutionary sequences are computed from the full evolution of He-rich progenitor stars through all the relevant stellar evolutionary phases, including the ZAMS, the RGB, the core He flash (whenver it occurs), the stable core He burning, the AGB phase and the entire TP- and post-AGB phases. Specifically, we present full evolutionary sequences for He-rich progenitors with masses ranging from  $0.6$  to  $2.0 M_{\odot}$ , and for an initial He abundance  $Y=0.4$ . These sequences are provided for two progenitor metallicities  $Z=0.001$  and  $Z=0.0005$ . To date, no such exploration of the evolution of He-rich stars exists in the literature, the only exception is that of Chantreau et al. (2015), who presented evolutionary sequences for He-rich progenitors for low-mass stars (up to  $1 M_{\odot}$ ) with  $Z=0.0005$  from the ZAMS to the end of the AGB phase, but did not compute the white dwarf stage. We emphasize that the computation of the entire evolutionary history of progenitor stars allows us to have self-consistent white dwarf initial models. That means that in our sequences the residual masses of the H-rich envelopes and of the He shells are obtained from evolutionary calculations, instead of using typical values and artificial initial white dwarf models. For the white dwarf regime, we have included all the relevant energy sources and physical processes such as crystallization, carbon-oxygen phase separation, element diffusion, residual nuclear burning, and convective coupling at low luminosities (Fontaine et al. 2001). As it will be shown below, the final mass of the remnants, the role of overshooting during the thermally-pulsing AGB, and the cooling properties of white dwarfs markedly differ from those corresponding to progenitor stars with the standard initial He abundance.

The paper is organized as follows. In Sect. 2 we briefly describe our numerical tools and the main ingredients of the evolutionary sequences, while in Sect. 3 we present in detail our main evolutionary results for both the white dwarfs and their progenitor. In this section we also explore the pulsational properties of the resulting white dwarfs during the ZZ Ceti stage. Finally, in Sect. 4 we summarize the main findings of the paper, and we elaborate on our conclusions.

## 2. Numerical setup and input physics

The evolutionary sequences presented here have been calculated with the LPCODE stellar evolutionary code – see Althaus et al. (2003), Althaus et al. (2005), Althaus et al. (2012), Althaus et al. (2015), and Miller Bertolami (2016) for relevant information about the code. LPCODE is a well-tested

and calibrated code that has been amply used to study different aspects of the evolution of low-mass and white dwarf stars, including the formation and evolution of extremely low-mass white dwarfs – see Miller Bertolami et al. (2008), García-Berro et al. (2010), Althaus et al. (2010a), Renedo et al. (2010), Miller Bertolami et al. (2011), Wachlin et al. (2011), Córscico et al. (2012), and Althaus et al. (2013), and references therein. Recently, it has been used as well to generate a new grid of models for post-AGB stars (Miller Bertolami 2016). LPCODE has been tested against other evolutionary codes during the main sequence, RGB, and white dwarf regime (Salaris et al. 2013; Miller Bertolami 2016) with satisfactory results.

Next we provide a description of the main input physics of the code relevant for the present work. Extra mixing due to diffusive convective overshooting has been considered during the core H and He burning, but not during the thermally-pulsing AGB phase. The nuclear network accounts for the following elements:  $^1\text{H}$ ,  $^2\text{H}$ ,  $^3\text{He}$ ,  $^4\text{He}$ ,  $^7\text{Li}$ ,  $^7\text{Be}$ ,  $^{12}\text{C}$ ,  $^{13}\text{C}$ ,  $^{14}\text{N}$ ,  $^{15}\text{N}$ ,  $^{16}\text{O}$ ,  $^{17}\text{O}$ ,  $^{18}\text{O}$ ,  $^{19}\text{F}$ ,  $^{20}\text{Ne}$  and  $^{22}\text{Ne}$ , together with 34 thermonuclear reaction rates for the pp-chains, CNO bi-cycle, and He burning that are identical to those described in Althaus et al. (2005), with the exception of the reactions  $^{12}\text{C} + \text{p} \rightarrow ^{13}\text{N} + \gamma \rightarrow ^{13}\text{C} + \text{e}^+ + \nu_{\text{e}}$  and  $^{13}\text{C}(\text{p},\gamma)^{14}\text{N}$ , which are taken from Angulo et al. (1999). In addition, the reaction rate  $^{14}\text{N}(\text{p},\gamma)^{15}\text{O}$  was taken from Imbriani et al. (2005). Radiative and conductive opacities are computed using the OPAL tables (Iglesias & Rogers 1996) and adopting the treatment of Cassisi et al. (2007), respectively. The equation of state during the main sequence evolution is that of OPAL for H- and He-rich compositions and a given metallicity. Updated low-temperature molecular opacities with varying carbon-oxygen ratios are used, which is relevant for a realistic treatment of progenitor evolution during the thermally-pulsing AGB phase (Weiss & Ferguson 2009). For this purpose, we have adopted the low-temperature opacities of Ferguson et al. (2005) and Weiss & Ferguson (2009). For the white dwarf phase, we consider the equation of state of Magni & Mazzitelli (1979) for the low-density regime, while for the high-density regime, we employ the equation of state of Segretain et al. (1994). As the white dwarf cools down we take into account the effects of element diffusion due to gravitational settling, chemical and thermal diffusion of  $^1\text{H}$ ,  $^3\text{He}$ ,  $^4\text{He}$ ,

$^{12}\text{C}$ ,  $^{13}\text{C}$ ,  $^{14}\text{N}$  and  $^{16}\text{O}$  – see Althaus et al. (2003) for details. During the white dwarf regime and for effective temperatures smaller than  $10,000$  K, outer boundary conditions are derived from non-grey model atmospheres (Rohrmann et al. 2012). Energy sources resulting from nuclear burning, the release of latent heat of crystallization, as well as the release of the gravitational energy associated with the C/O phase separation induced by crystallization are also taken into account during this phase.

In the present work special care has been considered in computing the evolution along the TP-AGB phase. This is relevant for a correct assessment of the initial-to-final mass relation as well as for a realistic inference of the role of residual nuclear burning in cool white dwarfs (Althaus et al. 2015). In particular, we have not forced our sequences to abandon early the TP-AGB phase. As mentioned, overshooting was not taken into account during the TP-AGB phase. This assumption leads to upper limits to the final mass of the progenitor stars. Indeed, the inclusion of overshooting during this phase results in third dredge up episodes, that prevent the growth of the H-free core (Salaris et al. 2009). Unlike the situation for metal-rich progenitors, evidence for the occurrence of extra-mixing episodes during the TP-AGB phase of low-mass, low-metallicity stars is not conclusive (Althaus et al. 2015). To assess the impact of the oc-

**Table 1.** Basic model properties for sequences with  $Y=0.4$  and  $Z=0.001$  and  $0.0005$ .

| $M_{\text{ZAMS}} (M_{\odot})$ | $t_{\text{RGB}} (\text{Gyr})$ | $M_{\text{WD}} (M_{\odot})$ | $N_{\text{TP}}$                 | Evolutionary path                                       |
|-------------------------------|-------------------------------|-----------------------------|---------------------------------|---|
| $Y=0.4, Z=0.001$              |                               |                             |                                 |   |
| 0.60                          | 14.15                         | 0.4336                      | 0                               | He-core   |
| 0.65                          | 10.57                         | 0.450                       | 0                               | He-core   |
| 0.70                          | 8.08                          | 0.4894                      | 4 (at high $T_{\text{eff}}$ )   | Hot HB $\rightarrow$ AGB Manqu  $\rightarrow$ C/O WD    |
| 0.75                          | 6.31                          | 0.52801                     | 2 (at high $T_{\text{eff}}$ )   | HB $\rightarrow$ TP-AGB Manqu  $\rightarrow$ C/O WD     |
| 0.80                          | 5.02                          | 0.55837                     | 2 (1 at high $T_{\text{eff}}$ ) | HB $\rightarrow$ TP-AGB $\rightarrow$ C/O WD            |
| 0.85                          | 4.09                          | 0.57982                     | 2                               | HB $\rightarrow$ TP-AGB $\rightarrow$ C/O WD            |
| 1.0                           | 2.35                          | 0.61561                     | 4                               | HB $\rightarrow$ TP-AGB $\rightarrow$ C/O WD            |
| 1.5                           | 0.648                         | 0.70424                     | 11                              | TP-AGB $\rightarrow$ C/O WD                             |
| 2.0                           | 0.31                          | 0.81114                     | 20                              | TP-AGB $\rightarrow$ C/O WD                             |
| $Y=0.4, Z=0.0005$             |                               |                             |                                 |   |
| 0.60                          | 13.49                         | 0.43968                     | 0                               | He-core   |
| 0.65                          | 10.08                         | 0.45746                     | 0                               | He-core   |
| 0.70                          | 7.72                          | 0.50053                     | 4 (at high $T_{\text{eff}}$ )   | Hot HB $\rightarrow$ TP-AGB Manqu  $\rightarrow$ C/O WD |
| 0.75                          | 6.038                         | 0.53385                     | 3 (1 at high $T_{\text{eff}}$ ) | HB $\rightarrow$ TP-AGB $\rightarrow$ C/O WD            |
| 0.85                          | 3.893                         | 0.58029                     | 3                               | HB $\rightarrow$ TP-AGB $\rightarrow$ C/O WD            |
| 1.0                           | 2.235                         | 0.62152                     | 5                               | HB $\rightarrow$ TP-AGB $\rightarrow$ C/O WD            |
| 1.5                           | 0.626                         | 0.71232                     | 12                              | TP-AGB $\rightarrow$ C/O WD                             |
| 2.0                           | 0.293                         | 0.83789                     | 24                              | TP-AGB $\rightarrow$ C/O WD                             |

**Notes.**  $M_{\text{ZAMS}}$ : initial mass,  $t_{\text{RGB}}$ : age at the RGB (in Gyr),  $M_{\text{WD}}$ : white dwarf mass,  $N_{\text{TP}}$ : number of thermal pulses. The last column gives the evolutionary path followed by the star.

currence of extra-mixing in the TP-AGB phase, particularly on the final mass of progenitors and the role of residual nuclear burning during the white dwarf regime, we compute additional He-rich sequences in which we considered an exponentially decaying diffusive overshooting with the overshooting parameter set to  $f=0.0075$ . As shown in Miller Bertolami (2016), this amount of overshooting reproduces many observational properties of AGB and post-AGB stars such as the C/O ratios of AGB and post-AGB stars in the Galactic Disk, C/O abundances in PG 1159 stars, and the mass range of C-rich stars in the clusters of the Magellanic Clouds.

In this work, mass loss during the RGB was taken from Schr der & Cuntz (2005). Although this election is an acceptable choice, it should be stressed, however, that the RGB mass-loss law is uncertain, and particularly its dependence on the initial helium abundance is still unknown. For the AGB and TP-AGB phases, we use again the mass loss rate of Schr der & Cuntz (2005) for pulsation periods shorter than 50 days. For longer periods, mass loss is taken as the maximum of the rates of Schr der & Cuntz (2005) and Groenewegen et al. (2009) for oxygen-rich stars, or the maximum of the rates of Schr der & Cuntz (2005) and Groenewegen et al. (1998) for carbon-rich stars. In all of our calculations, mass loss was suppressed after the post-AGB remnants reach  $\log T_{\text{eff}}=4$ . In line with the findings of Cassisi et al. (2014), who reported that no enhanced mass loss should be expected in second generation HB stars, we assume no mass loss during the core He-burning phase on the HB.

We computed the full evolution of He-rich sequences with initial masses ranging from 0.6 to  $2.0 M_{\odot}$ . The initial He abundance of each sequence is  $Y=0.4$ . Two sets of model sequences have been computed, one for metallicity  $Z=0.001$  and the other one for  $Z = 0.0005$ . It is important to mention that the value of the initial helium abundance adopted here constitutes an extreme choice. In fact, only  $\omega$  Centauri and NGC 2808 show evidence of sub-populations with such high large helium abundances, while the sub-populations of most typical clusters are characterized by helium abundances generally  $\lesssim 0.3$  (Bastian et al. 2015). A description of the computed evolutionary sequences is provided

in Table 1, which lists the initial mass of our sequences and the final white dwarf mass (in solar masses), together with the age (in Gyr) at the end of the RGB and the number of thermal pulses. The adopted metallicities are representative of the low-metal content of the second generation, He-rich population found in some globular clusters. In particular, Tailo et al. (2016) find that the metallicity of the He-rich population in  $\omega$  Centauri is  $Z = 0.0006 - 0.001$ , and  $Y \sim 0.38$ . For all our sequences, evolution has been computed starting from the ZAMS and followed through the stages of stable H and He core burning, the stage of mass loss during the entire TP-AGB, the domain of the planetary nebulae at high effective temperature, and finally the terminal white dwarf cooling track, until very low surface luminosities ( $\log(L/L_{\odot}) = -5.0$ ). For most of our sequences, evolution has gone through the He core flash on the tip of the RGB, and the following recurrent sub-flashes, before the progenitors reach the stable core He-burning stage on the HB.

### 3. Evolutionary results

In this work we will focus on those aspects of the evolution of stars with enhanced initial helium abundances which are relevant for the formation and evolution of white dwarf stars. Other issues such as the impact of the helium enhancement of the progenitor stars on the morphology of HB stars, on the existence of multiple populations in globular clusters, or on the consequences of the helium enhancement on the evolution and nucleosynthesis of AGB models can be found in D’Antona et al. (2002), Charbonnel et al. (2013), Milone (2015), Shingles et al. (2015), and references therein.

#### 3.1. The evolution of white dwarf progenitors

It is well known that stars with an enhanced helium abundance have much shorter main sequence lifetimes for a given initial mass than stars with a normal helium abundance. This is the logical consequence of a smaller hydrogen mass to burned on the main sequence. However this is not the only reason for this

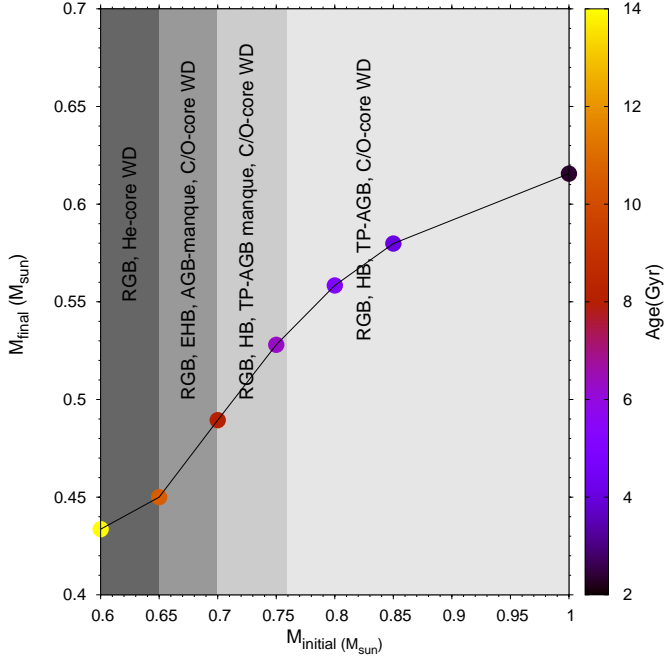


**Fig. 1.** Theoretical initial-to-final mass relationship and evolutionary stages (shown employing different gray scales) obtained following the evolution of stars with an initial helium-enhanced composition  $Y=0.4$  and a metallicity  $Z=0.001$ . The color scale on the right shows the age (in Gyr) at the tip of the RGB.

behavior. Specifically, in the hydrogen burning core the mean molecular weight is larger. All in all, stars with enhanced helium abundances are brighter and hotter for a given mass, see Salaris & Cassisi (2005) and Charbonnel et al. (2013). Indeed, as can be noted in Table 1, progenitors with initial stellar masses as low as  $M \approx 0.60 M_{\odot}$  reach the tip of the RGB in less than 14 Gyr. In addition, because of the larger temperature characterizing the hydrogen-exhausted core during the RGB, the helium flash for these stars occurs for lower helium core masses than for stars with normal helium abundances.

These facts have consequences for the initial-to-final mass relationship, as well as for the global evolution of these stars. This is illustrated in Fig. 1, where the initial-to-final mass relation for our less massive helium-enhanced evolutionary sequences is shown for the case  $Z=0.001$ . In this figure the evolution paths of these stars according to their initial mass is also indicated. In particular, progenitors with initial mass less than  $M \approx 0.65 M_{\odot}$  do not evolve through the helium core flash at the tip of the RGB. Instead, they evolve directly to the white dwarf stage. For these progenitors, helium-core white dwarfs are formed in less than 14 Gyr (see Table 1). Our sequences with initial stellar masses larger than  $M \approx 0.65 M_{\odot}$  end their lives forming white dwarfs with C/O cores. Specifically, helium-enhanced stars with initial stellar masses within the range  $0.65 \lesssim M_{\odot} \lesssim 1.0$  evolve through the helium core flash and then to the HB. It is worth noting that those progenitors with masses in the interval  $0.65 \lesssim M_{\odot} \lesssim 0.70$  avoid the AGB phase (AGB manqué), and evolve directly to the cooling sequence as C/O white dwarfs – see Chantreau et al. (2015) for a similar result – while those progenitors with  $0.70 \lesssim M_{\odot} \lesssim 0.75$  reach the AGB phase but not the thermally pulsing AGB phase (TP-AGB manqué).

In our simulations, only those progenitors with initial stellar mass larger than  $\approx 0.70 M_{\odot}$  are able to reach the AGB

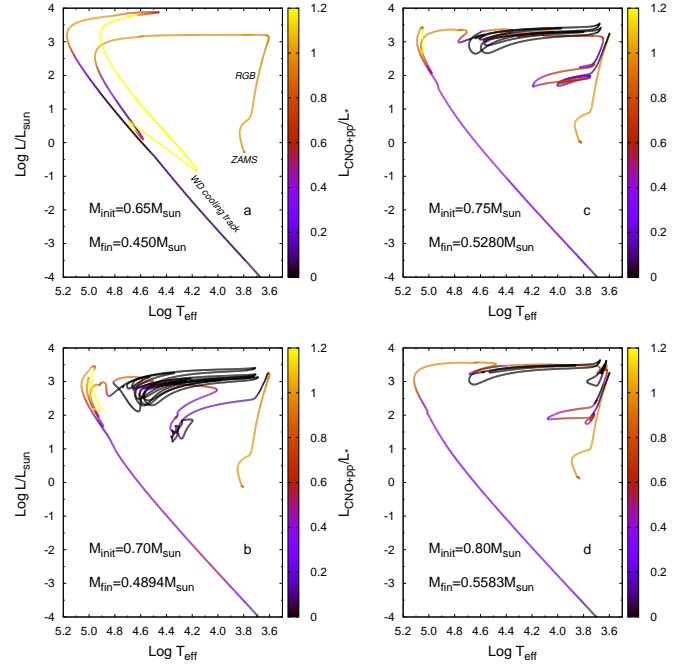


**Fig. 2.** Hertzsprung-Russell diagram for our helium-enhanced evolutionary sequences for metallicity  $Z=0.001$  and initial helium mass fraction  $Y = 0.4$ . Evolutionary tracks for progenitors with initial stellar mass of  $0.65 M_{\odot}$ ,  $0.70 M_{\odot}$ ,  $0.75 M_{\odot}$ , and  $0.80 M_{\odot}$  (panels a,b,c, and d, respectively) are depicted from the ZAMS to advanced stages of white dwarf evolution. The color scale on the right shows the fraction of the total luminosity due to hydrogen burning. The upper value of the color scale has been set to 1.2, so larger values of  $L_{\text{CNO+pp}}/L_*$  are not shown.

phase. This is in good agreement with the calculations of Charbonnel et al. (2013). This is clearly illustrated in Figs. 2 and 3, which display the evolution in the Hertzsprung-Russell diagram of some selected sequences with  $Z=0.001$ , from the ZAMS to the white dwarf stage. The color scale in each figure shows the fraction of the total luminosity due to hydrogen burning. Note that the sequence with initial mass  $M = 0.70 M_{\odot}$  (panel b in Fig. 2) evolves directly to the white dwarf regime without passing through the AGB phase (AGB manqué). Indeed, this sequence, that experiences the core helium flash shortly after departing from the RGB phase, settles onto the hot HB (at  $T_{\text{eff}} = 22,400\text{K}$ ) to burn helium in a stable way. Because of its very thin hydrogen envelope, this sequence does not go through the AGB phase after the end of core helium burning. On the other hand, the sequence with initial mass  $M = 0.75 M_{\odot}$  (panel c in Fig. 2) reaches the AGB but abandons it before reaching the TP-AGB phase (TP-AGB manqué). However, note that both sequences experience several helium shell flashes before reaching the white dwarf regime.

Panel a in Fig. 2 shows the complete evolution of our progenitor star of mass  $M = 0.65 M_{\odot}$  that ends its life as a helium-core white dwarf of mass  $M = 0.45 M_{\odot}$ . Before reaching the terminal cooling track, this sequence experiences a CNO shell flash, that reduces the effects of residual hydrogen burning on its evolution at late cooling times. This is in contrast with the expectation for very massive helium-core white dwarfs resulting from progenitors with standard initial helium abundances. In this case, CNO flashes are not expected to occur, as reported in Serenelli et al. (2002) and Althaus et al. (2013). The occur-

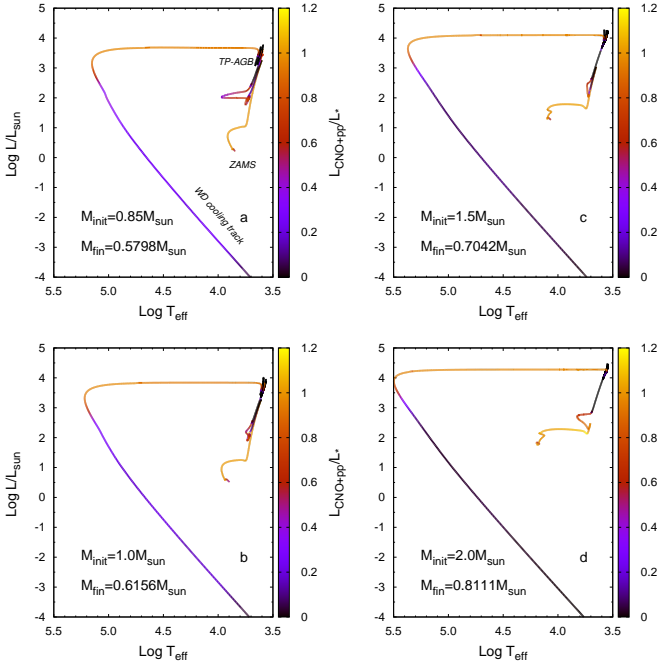


**Fig. 3.** Same as Fig. 2 but for the evolutionary sequences of stars with masses  $0.85 M_{\odot}$ ,  $1.0 M_{\odot}$ ,  $1.5 M_{\odot}$ , and  $2.0 M_{\odot}$ .

rence or not of a CNO shell flash is critical for the cooling times of these stars. Finally, note from Figs. 2 and 3 that, except for the more massive white dwarf sequences and for the helium-core ones, residual hydrogen burning constitutes a main energy source for all the resulting white dwarfs, also at advanced stages of evolution (see later in this section).

The impact of the initial helium content on the resulting final mass is shown in Fig. 4, which displays the theoretical initial-to-final mass relation resulting for our helium-enhanced evolutionary sequences for metallicity  $Z=0.001$  and  $Z=0.0005$ . The final mass is the stellar mass with which the remnant enters the white dwarf phase. The figure also shows the mass of the hydrogen-free core (HFC) at the first thermal pulse for the case in which  $Y=0.4$  and  $Z=0.001$  are adopted. For the sake of comparison, we also include in the figure the initial-final-mass relation for sequences that do not consider a helium enhancement. In particular, we plot, using a green solid line, the resulting relationship for the case  $Y=0.247$ ,  $Z=0.001$  (Althaus et al. 2015). The growth of the HFC mass during the TP-AGB, i.e. beyond the first thermal pulse, is evident for initial masses larger than  $M \sim 1.0 M_{\odot}$ . Because of the small amount of mass remaining above the HFC at the first thermal pulse, the final mass for the less massive sequences does not differ appreciably from the mass of the HFC at the first thermal pulse.

It is also worth noting in this figure that in the case of helium-enhanced sequences, the final mass of the remnants is markedly larger than the final mass expected from sequences with a standard initial abundance of helium. This can be understood by examining Fig. 5, which displays the temporal evolution of the mass of the HFC from the onset of core helium burning to the moment at which the first thermal pulse is reached for the  $1.0 M_{\odot}$ ,  $Z=0.001$  sequences in which  $Y=0.4$  and  $Y=0.247$  are considered. The color scale on the right of the figure shows the core helium abundance. Despite the HFC mass before the onset of core helium burning is smaller for the helium-enhanced sequence, it grows more rapidly during the helium burning phase

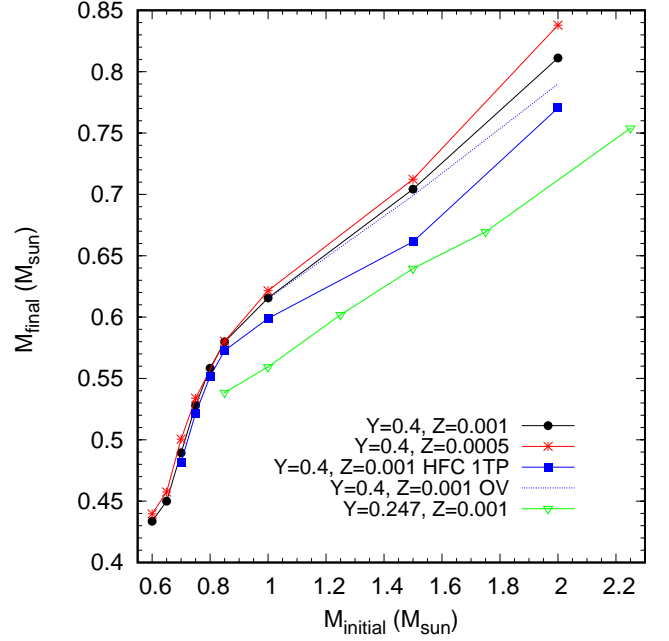


**Fig. 4.** Theoretical initial-to-final mass relation for our helium-enhanced evolutionary sequences with metallicity  $Z=0.001$  and  $Z=0.0005$  (black and red solid lines, respectively). We also show the mass of the HFC at the first thermal pulse for the case  $Y=0.4$ ,  $Z=0.001$  (blue solid line). In addition, the initial-to-final mass relation when overshooting is considered during the TP-AGB phase, and that resulting from sequences with standard helium content ( $Y=0.247$  and  $Z=0.001$ ) are also shown (blue dotted and green solid lines, respectively).

than in the case in which a standard initial helium abundance is considered. This is because hydrogen burning by the CNO cycle is more efficient in the helium-enhanced sequence. Thus, after helium exhaustion in the core, the helium-enhanced sequence ends up with a larger HFC.

We now compare the predictions for the final mass of our sequences with those of Chantereau et al. (2015). In particular, we pay special attention to the  $0.8 M_{\odot}$ ,  $Z=0.0005$  sequence studied in detail by these authors. As can be seen in Fig. 4 for our  $0.8 M_{\odot}$ ,  $Z=0.0005$  progenitor we obtain a mass of  $\sim 0.56 M_{\odot}$ , which is markedly smaller than that derived by Chantereau et al. (2015) for the same initial helium abundance,  $0.659 M_{\odot}$ . This discrepancy is mostly due to the different mass-loss rates used in both studies, particularly during the AGB and early TP-AGB phases. In fact, as mentioned in Sect. 2, for those phases we rely on the mass-loss formulation of Schröder & Cuntz (2005) – which is the same we use for the RGB phase. In contrast, Chantereau et al. (2015) employed the mass-loss rate of Vassiliadis & Wood (1993) after the end of core-helium burning. This treatment predicts mass-loss rates substantially smaller than those of Schröder & Cuntz (2005) during these phases. This is particularly true for low-mass stars. This results in a larger number of thermal pulses and a larger final mass when compared with those obtained using our prescriptions. To check this, we have re-computed our  $0.85 M_{\odot}$ ,  $Z=0.0005$  sequence, but now using the mass-loss rate of Vassiliadis & Wood (1993) after the end of helium core burning. During the AGB and early TP-AGB, the mass-loss rates are between 2 and 3 orders of magnitude smaller than those



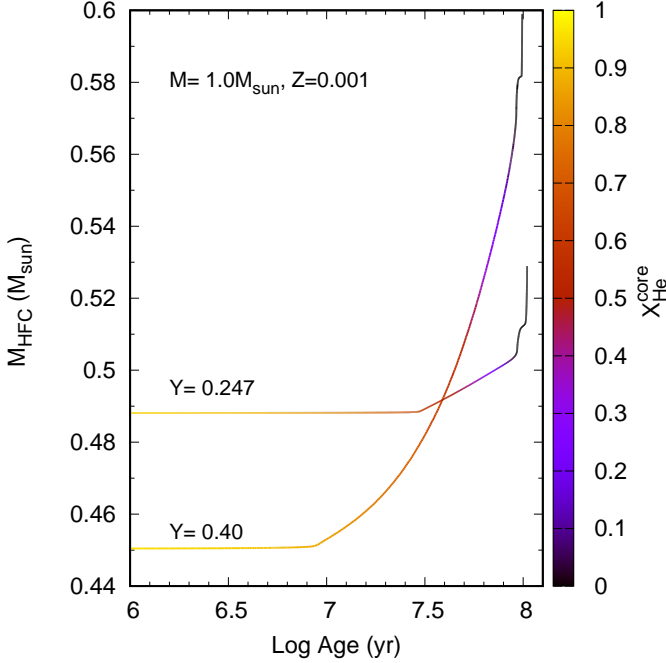


**Fig. 5.** Time evolution of the mass of the HFC from the onset of core helium burning until the occurrence of the first thermal pulse for the  $1.0 M_{\odot}$ ,  $Z=0.001$  sequences with  $Y=0.4$  and  $Y=0.247$ . The color scale on the right shows the core helium abundance (mass fraction). Note the substantial increase of the HFC mass during core helium burning for the helium-enhanced sequence.

given by Schröder & Cuntz (2005). As a result, our sequence experiences many more thermal pulses (20) and ends its evolution with a final mass of  $0.675 M_{\odot}$ , markedly larger than the final mass of  $0.58 M_{\odot}$  we find when the prescription of Schröder & Cuntz (2005) is used. This explains the much larger final mass found in Chantreau et al. (2015), as compared with that obtained here. However, we mention that for the AGB phase, the prescription of Vassiliadis & Wood (1993) yields a mass-loss rate much smaller than expected for the RGB phase. This contradicts the mass-loss estimates obtained for stars in  $\omega$  Centauri (McDonald et al. 2009). For instance, at  $\log(L/L_{\odot}) = 3.0$  on the AGB the prescription of Vassiliadis & Wood (1993) yields a mass-loss rate three orders of magnitude times smaller than that of Schröder & Cuntz (2005) for the RGB at the same luminosity. Also, Rosenfield et al. (2014) have shown that the mass-loss rates of Schröder & Cuntz (2005) provide a consistent description of pre-dust AGB winds.

The theoretical initial-to-final mass relations shown in Fig. 4 correspond to evolutionary sequences for which overshooting was disregarded during the TP-AGB phase. For all of these sequences, we did not find third dredge-up episodes. However, at low metallicities overshooting favors the occurrence of third dredge-up episodes and carbon enrichment of the envelope also for very small stellar masses (Weiss & Ferguson 2009). Nevertheless, there is no conclusive evidence about the occurrence of third dredge-up episodes in metal-poor, low-mass progenitors (Althaus et al. 2015). To assess the impact of overshooting during the TP-AGB on the final mass of the remnant we have re-computed some of our sequences for  $Y=0.4$ ,  $Z=0.001$  but allowing overshooting from the beginning of the thermally-pulsing AGB phase. Results are depicted in Fig. 4 with a blue

dotted line. Following Miller Bertolami (2016), we considered diffusive overshooting with the overshooting parameter set to  $f=0.0075$  – see Renedo et al. (2010); Weiss & Ferguson (2009) for details. As shown in Miller Bertolami (2016), and mentioned in Sect. 2, the choice of  $f=0.0075$  reproduces several observational properties of AGB and post-AGB stars in our Galaxy and in the Magellanic Clouds. The occurrence of third dredge-up episodes in the sequences with overshooting reduce further growth of the HFC, thus yielding lower final masses. Also, the increase in the C/O ratio resulting from a third dredge-up episode results in cooler stars. This, in turn, translates in significantly larger mass-loss rates. As a result, the remnant of the evolution departs from the AGB after a few more thermal pulses following the occurrence of third dredge-up. We find that only our  $1.5$  and  $2.0 M_{\odot}$  sequences experience third dredge-up. In particular, for the  $2.0 M_{\odot}$  sequence,  $C/O > 1$  after the third thermal pulse, and becomes  $C/O > 2.5$  after the tenth thermal pulse. From Fig. 4 we conclude that the initial-to-final mass relation for helium-enhanced stars is not markedly modified by the occurrence of overshooting during the TP-AGB phase.

### 3.2. The evolution of white dwarfs

We now pay attention to the evolution of white dwarfs resulting from helium-enhanced progenitors. We begin examining Fig. 6, where we plot the fraction of the total white dwarf luminosity due to hydrogen nuclear burning (CNO and  $pp$  burning) during the entire cooling phase for all our helium-enhanced evolutionary sequences of metallicity  $Z=0.0005$  and  $Z=0.001$ , upper and bottom panels, respectively, and initial helium mass fraction  $Y=0.4$ . In this figure, the red lines show the predictions for those sequences that end as helium-core white dwarfs, whilst blue lines depict the results for those sequences which result in white dwarfs with C/O cores. In addition, in the bottom panel of this figure we include the prediction for a helium-core white dwarf sequence of mass  $0.435 M_{\odot}$  resulting from the evolution of a progenitor with  $Z=0.01$  and standard initial helium abundance (Althaus et al. 2013). Note that, for the less massive C/O white dwarfs, residual hydrogen burning becomes a main energy source even at low luminosities. This is in line with the results of Miller Bertolami et al. (2013) and Althaus et al. (2015), who found that low-mass white dwarfs resulting from low-metallicity progenitors that have not experienced third dredge-up, are characterized by massive hydrogen envelopes. This, in turn, has one evident effect, namely that residual hydrogen burning becomes one of the main energy sources during the evolution of white dwarfs for substantial periods of time. The calculations performed here show that this is also true for white dwarfs resulting from helium-enhanced progenitors.

As shown in Althaus et al. (2015), see also Miller Bertolami (2016), for low-mass, low-metallicity progenitor stars overshooting during the TP-AGB phase leads to carbon enrichment of the envelope due to third dredge-up episodes, and consequently reduces the final mass of the hydrogen envelope with which the corresponding white dwarfs enter into their cooling track. This, obviously, minimizes the role played by residual hydrogen burning. Hence, the conclusion reached by Althaus et al. (2015) and Miller Bertolami (2016) that residual hydrogen burning impacts the cooling of low-metallicity white dwarfs is not valid if some amount of overshooting is allowed during the TP-AGB phase of low-mass progenitors. This is in contrast with the situation we find for white dwarfs resulting from helium-enhanced progenitors. In fact, as mentioned previously, when overshooting is considered during the TP-AGB phase of helium-

enhanced progenitors third dredge-up only occurs for our more massive sequences. For the less massive ones, no carbon enrichment is predicted when overshooting is considered, and consequently residual hydrogen burning plays a role in the evolution of the resulting white dwarfs. To summarize, the conclusion that stable hydrogen burning dominates a significant part of the evolution of low-mass white dwarfs resulting from low-metallicity He-enhanced progenitors does not depend on the occurrence of overshooting during the TP-AGB evolution.

Another interesting feature of the results shown in Fig. 6 is the small impact of residual hydrogen burning on the evolution of massive helium-core white dwarfs resulting from helium-enhanced progenitors. Again, this is because these white dwarfs experience a CNO shell flash during the cooling branch that reduces the mass of the residual hydrogen-rich envelope, thus minimizing the role of hydrogen burning at advanced stages of the evolution. This is in contrast with what occurs for helium-core white dwarfs resulting from progenitors with standard initial helium abundances – see Istrate et al. (2014) and Althaus et al. (2013) for recent works – since for very massive helium-core white dwarfs CNO flashes do not occur, even when element diffusion is taken into account. To illustrate this in Fig. 6 we show, using a thick green line, the contribution of residual hydrogen burning for a helium-core white dwarf of mass  $0.435 M_{\odot}$  resulting from a progenitor star with  $Z=0.01$  and a standard initial helium abundance (Althaus et al. 2013). For this star, no CNO flashes took place, and thus in this case, hydrogen burning contributes significantly to the luminosity of the white dwarf.

The resulting cooling times are displayed in Fig. 7. This figure shows the cooling times of our sequences for helium-enhanced progenitors with  $Z=0.001$ ,  $Y=0.4$ . The time origin is taken at the moment at which the remnants reach the point of maximum effective temperature at the beginning of the cooling branch. As in Fig. 6, we show with blue lines, the results for white dwarfs with C/O cores, and with red lines, those for white dwarfs with helium cores. We find that residual nuclear burning yields substantial delays in the cooling time for the less massive C/O white dwarfs. At  $\log(L/L_{\odot}) \sim -3.0$ , residual hydrogen burning leads to an increase in the cooling times of low-mass white dwarfs which ranges between 20 and 40%. This conclusion is independent of the assumed initial helium abundance. In fact, Althaus et al. (2015) found a similar result for the case of white dwarfs resulting from progenitors with standard helium abundances. However, as mentioned earlier, in contrast with what is found for the case of standard sequences, the impact of residual hydrogen burning on the cooling times of low-mass white dwarfs resulting from helium-enhanced progenitors is not affected by the occurrence of overshooting on the TP-AGB phase of their progenitor stars.

The initial helium abundance also impacts the evolution of helium-core white dwarfs. To show this, in Fig. 7 we include the cooling curves for a helium-core white dwarf of mass  $0.435 M_{\odot}$  resulting from a progenitor with  $Z=0.01$  and standard initial helium abundance (Althaus et al. 2013), and for a helium-core white dwarf of mass  $0.449 M_{\odot}$  resulting from a progenitor with  $Z=0.001$  and a standard initial helium abundance (Serenelli et al. 2002), solid and dashed green lines, respectively. Note that the helium-core white dwarf resulting from helium-enhanced progenitors evolves much faster than their counterparts resulting from standard progenitors. As mentioned, this different behavior is due to the occurrence of a CNO shell flash in the helium-core white dwarf with helium-enhanced progenitors that reduces the impact of further nuclear burning at advanced stages. In fact, at intermediate and low luminosities, the cooling times of massive

helium-core white dwarfs with helium-enhanced progenitors are about a factor of 2 shorter, when compared with the helium-core white dwarfs formed from progenitors with standard initial helium abundances.

### 3.3. The pulsational properties

As already shown, the helium enhancement of progenitor stars has a significant impact on the formation and evolution of the resulting white dwarfs. In this sense, it is worthwhile to also explore the pulsational properties of these white dwarfs. The pulsational properties of these stars are strongly dependent on the shape of the chemical profile left by the evolution of their progenitors. In this connection, in Fig. 8 we show, using thick lines, the inner abundance distribution of hydrogen, helium, carbon and oxygen as a function of the outer mass fraction for selected white dwarf models resulting from helium-enhanced progenitors with  $Z=0.001$  and initial helium abundance  $Y=0.4$  at the ZZ Ceti stage. In addition, the thin lines show the chemical profiles at the beginning of the cooling track. Panel a corresponds to a helium-core white dwarf that results from a progenitor of initial mass  $M = 0.65 M_{\odot}$ , while panels b, c, and d to C/O white dwarfs resulting from progenitors of masses  $M = 0.70 M_{\odot}$ ,  $M = 0.75 M_{\odot}$ , and  $M = 1.0 M_{\odot}$ , respectively. The carbon and oxygen profiles are the result of different processes acting during the evolution of the progenitor. In particular, note the flat profile in the inner core left by convection during the core helium burning phase and the signatures of the outward-moving helium burning shell, particularly for the more massive sequence illustrated, which reached the thermally pulsing AGB phase. In addition, the chemical profiles at the beginning of the cooling track of the C/O sequences show the typical intershell rich in helium and carbon left by the pulse-driven convection zone during the thermally pulsing phase. This intershell is present in all our C/O white dwarf sequences. We remind that although the  $M = 0.70 M_{\odot}$  and  $M = 0.75 M_{\odot}$  progenitors avoided the TP-AGB phase, they nonetheless experienced several thermal pulses at high effective temperatures before entering the white dwarf stage. The action of element diffusion is clearly also noticeable, and leads to the formation of a thick hydrogen envelope by the time evolution has reached the domain of the ZZ Ceti stars. But more importantly, it removes the double-layered structure at the interhell region for white dwarfs with masses larger than  $M \approx 0.60 M_{\odot}$ . For less massive white dwarfs, the intershell region is not removed by diffusion. In this regards, it is important to realize that the presence of a double-layered structure affects the theoretical  $g$ -mode period spectrum of ZZ Ceti stars, see Althaus et al. (2010a).

Once we have studied the chemical stratification of these white dwarf models we continue our analysis computing the adiabatic pulsation periods of nonradial  $g$  (gravity) modes employing the LP-PUL pulsation code described in Córscico & Althaus (2006). In Fig. 9 we show the propagation diagrams (Unno et al. 1989) corresponding to the same stellar models depicted in Fig. 8. The propagation diagrams are the spatial run of the Brunt-Väisälä (buoyancy) frequency,  $N$ , and the Lamb (acoustic) frequency,  $L_{\ell}$ . The shape of the Brunt-Väisälä frequency largely determines the properties of the  $g$ -mode pulsation spectrum (Winget & Kepler 2008; Fontaine & Brassard 2008; Althaus et al. 2010b). The profile of  $N$  reflects all changes in chemical composition of the white dwarf model in the form of local maxima of the buoyancy frequency (Unno et al. 1989). In the case of the helium-core white dwarf model, there exists only one chemical interface – the helium-hydrogen transition region

(see panel a of Fig. 8). This chemical interface induces a bump in  $N^2$  at  $-\log(1 - M_r/M_\star) \sim 3.5$  (panel a of Fig. 9). Note that this interface also affects the shape of the Lamb frequency. In the case of white dwarfs with carbon-oxygen cores, the internal chemical structure is substantially more complex than in the case of the helium-core white dwarf models (see panels b, c, and d in Fig. 8). This results in a much more complex form of the run  $N^2$ , as can be seen in panels b, c, and d of Fig. 9. Indeed, in these cases, the Brunt-Väisälä frequency is characterized by additional maxima induced by the presence of the C/O-He and the C/O chemical interfaces.

The number and shape of the chemical interfaces present in the interior of DA white dwarf models strongly affect the propagation properties of nonradial pulsation  $g$  modes, in particular through mode trapping and confinement (Brassard et al. 1992; Bradley 1996; Córscico et al. 2002). Mode-trapping or confinement results in strong departures from uniformity of the forward period separation,  $\Delta\Pi_k (\equiv \Pi_{k+1} - \Pi_k)$ , when plotted in terms of the pulsation period  $\Pi_k$  ( $k$  being the radial order of the mode). Thus, the period difference between an observed mode and adjacent modes can be considered as an observational diagnostic of mode trapping. For a helium-core white dwarf – characterized by a single chemical interface – like that of the model of mass  $M = 0.45M_\odot$  we are considering here, local minima in  $\Delta\Pi_k$  usually correspond to modes trapped in the hydrogen envelope, in contrast to local maxima in  $\Delta\Pi_k$ , which are associated with modes trapped in the inner core. The forward period spacing for  $\ell = 1$   $g$  modes in terms of the periods corresponding to the helium-core model of mass  $M = 0.45M_\odot$  is depicted in panel a of Fig. 10. We also show the asymptotic period spacing, computed as in Tassoul et al. (1990) with a dotted blue line. Mode-trapping signatures are clearly noticeable, particularly for periods shorter than  $\sim 1500$  s. Longer periods seem to fit the asymptotic predictions, although small departures from constant period spacing are still clearly seen. In the case of white dwarfs with carbon-oxygen cores, the presence of multiple chemical transition regions causes much more complex patterns of mode-trapping/confinement, as can be seen in panels b, c, and d of Fig. 10. In particular, strong departures from uniform period separation are evident for the models with  $M = 0.489M_\odot$ ,  $M = 0.528M_\odot$ , and  $M = 0.615M_\odot$ . These features persist for the entire range of periods analyzed here. We also note some “beating” modulating the amplitudes of the departures of  $\Delta\Pi_k$ . This beating is due to the combined mode-trapping/confinement effects caused by the various steps in the C/O profile in the core – see Córscico & Althaus (2006) for the case of PG1159 star models. Clearly, the mode trapping/confinement features of models with C/O cores are by far more pronounced than for the case of the helium-core white dwarf.

#### 4. Summary and conclusions

In this work we have computed the full evolution of helium-enhanced ( $Y=0.4$ ) sequences with initial masses ranging from  $0.60$  to  $2.0M_\odot$ . Two sets of model sequences have been computed, for the first one we adopted a metallicity  $Z=0.001$ , whereas for the second one  $Z=0.0005$  was employed. Emphasis has been placed on those aspects of evolution of helium-enhanced star relevant for the formation and evolution of white dwarfs. For all our sequences, evolution has been computed starting from the ZAMS and followed through the stages of stable hydrogen and helium core burning, the stage of mass loss during the entire thermally-pulsing AGB, the domain of the planetary nebulae at high effective temperature, and finally the

terminal white dwarf cooling track, up to very low surface luminosities. To the best of our knowledge, the sequences presented here constitute the first set of consistent evolutionary tracks from the ZAMS to the white dwarf stage covering a wide range of masses. This set of sequences is appropriate for the study of the formation and evolution of white dwarfs resulting from stars with very high initial helium abundances, like those found in  $\omega$  Centauri and NGC 2808.

We explored different aspects of the evolution of the resulting white dwarfs and of their progenitors. In particular, we studied the initial-to-final mass relation, and we found that the final mass of white dwarfs resulting from helium-enhanced progenitors is markedly larger than the final mass expected from sequences with a standard helium initial abundance. Progenitors with initial mass smaller than  $M \simeq 0.65M_\odot$  evolve directly into white dwarfs with helium cores in less than 14 Gyr, while those descending from more massive progenitors and with initial stellar mass smaller than  $M \simeq 0.75M_\odot$ , reach the white dwarf stage avoiding the TP-AGB phase, TP-AGB manquè (or AGB manquè if the stellar mass is less than  $M \simeq 0.70M_\odot$ ). However, before reaching the terminal cooling track, these remnants experience several helium thermal pulses at high effective temperatures. It is worth noting that the formation of helium-core white dwarfs in our simulations is not the result of binary evolution, but a consequence of the much shorter ages of the low-mass, helium-enhanced progenitors. This is in accordance with the results of Calamida et al. (2008), Cassisi et al. (2009), and Bellini et al. (2013a), who found evidence for the existence of an important fraction of helium-core white dwarfs in  $\omega$  Centauri.

Our simulations show that for initial masses larger than  $M \sim 1.0M_\odot$  the hydrogen-free core grows during the TP-AGB. For lower stellar masses, the final mass of the remnants of helium-enhanced progenitors does not differ appreciably from the mass of the hydrogen-free core at the first thermal pulse. We have also explored the impact of overshooting during the TP-AGB, and found that the occurrence of third dredge-up and the related carbon enrichment of the envelope is expected to occur for initial masses larger than  $\sim 1.5M_\odot$ . However, we found that the initial-to-final mass relation for helium-enhanced stars is not markedly altered by the occurrence of overshooting during the TP-AGB phase.

With regard to the evolution of the resulting white dwarfs, we find that for the less massive C/O white dwarfs, residual hydrogen burning becomes a main energy source even at low luminosities, in agreement with the predictions of Althaus et al. (2015), who found that low-mass white dwarfs resulting from low-metallicity progenitors that have not experienced third dredge-up, are characterized by residual hydrogen burning, so this energy source dominates the evolution for substantial periods of time. The resulting delays in the cooling times range from 20 to 40% at low luminosities. However, in contrast with the situation encountered for white dwarfs resulting from standard progenitors, we found that the role played by stable hydrogen burning in low-mass white dwarfs descending from helium-enhanced progenitors does not depend on the occurrence of overshooting during the TP-AGB evolution. In addition, according to our simulations, the very massive helium-core white dwarfs descending from helium-enhanced progenitors experience a CNO shell flash during the cooling branch, thus minimizing the impact of hydrogen burning at advanced stages of the evolution. As a consequence, at intermediate and low luminosities, cooling times of massive helium-core white dwarfs formed from helium-enhanced progenitors are about a factor of 2 lower, as compared with helium-



core white dwarfs resulting from progenitors with a standard initial helium abundance.

We also find that a double-layered structure in the outer chemical profile is formed in all the resulting C/O models. This double-layered chemical profile is the result of the mixing in the pulse-driven convection zone that appears as a result of the helium thermal pulses. However, by the time the ZZ Ceti regime is reached, this structure is removed by element diffusion for masses larger than  $M \simeq 0.60 M_{\odot}$ . This behavior impacts the pulsational properties of the models at the ZZ Ceti stage.

Finally, the pulsational properties of our models have been explored. We have found that in the case of white dwarfs with carbon-oxygen cores, the shape of the Brunt-Väisälä frequency is substantially more complex than in the case of white dwarfs with helium cores. This leads to a markedly different behavior of the mode-trapping/confinement properties and the forward period separation,  $\Delta\Pi_k (\equiv \Pi_{k+1} - \Pi_k)$ . In spite of the similarity of the stellar masses analyzed here, the mode trapping/confinement features of models with C/O cores are substantially different from those models with helium cores. Then, if pulsations are detected in future photometric observations in this type of objects, this distinctive difference in the  $\Delta\Pi_k$  distribution could be employed as a seismic diagnostic tool to distinguish white dwarfs with helium cores from those with C/O cores, provided that enough consecutive pulsation periods of  $g$  modes were detected. This constitutes a promising avenue to constrain the evolutionary history of cluster stars.

**Acknowledgements.** We thank our referee for his/her valuable comments. Part of this work was supported by AGENCIA through the Programa de Modernización Tecnológica BID 1728/OC-AR, by the PIP 112-200801-00940 grant from CONICET, by MINECO grant AYA2014-59084-P, and by the AGAUR. This research has made use of NASA Astrophysics Data System.

## References

- Althaus, L. G., Camisassa, M. E., Miller Bertolami, M. M., Córscico, A. H., & García-Berro, E. 2015, *A&A*, 576, A9
- Althaus, L. G., Córscico, A. H., Bischoff-Kim, A., et al. 2010a, *ApJ*, 717, 897
- Althaus, L. G., Córscico, A. H., Isern, J., & García-Berro, E. 2010b, *A&A Rev.*, 18, 471
- Althaus, L. G., García-Berro, E., Isern, J., Córscico, A. H., & Miller Bertolami, M. M. 2012, *A&A*, 537, A33
- Althaus, L. G., Miller Bertolami, M. M., & Córscico, A. H. 2013, *A&A*, 557, A19
- Althaus, L. G., Serenelli, A. M., Córscico, A. H., & Montgomery, M. H. 2003, *A&A*, 404, 593
- Althaus, L. G., Serenelli, A. M., Panei, J. A., et al. 2005, *A&A*, 435, 631
- Angulo, C., Arnould, M., Rayet, M., et al. 1999, *Nuclear Physics A*, 656, 3
- Bastian, N., Cabrera-Ziri, I., & Salaris, M. 2015, *MNRAS*, 449, 3333
- Bellini, A., Anderson, J., Salaris, M., et al. 2013a, *ApJ*, 769, L32
- Bellini, A., Piotto, G., Milone, A. P., et al. 2013b, *ApJ*, 765, 32
- Bono, G., Salaris, M., & Gilmozzi, R. 2013, *A&A*, 549, A102
- Bradley, P. A. 1996, *ApJ*, 468, 350
- Brassard, P., Fontaine, G., Wesemael, F., & Hansen, C. J. 1992, *ApJS*, 80, 369
- Calamida, A., Corsi, C. E., Bono, G., et al. 2008, *ApJ*, 673, L29
- Caloi, V. & D'Antona, F. 2007, *A&A*, 463, 949
- Cassisi, S., Potekhin, A. Y., Pietrinferni, A., Catelan, M., & Salaris, M. 2007, *ApJ*, 661, 1094
- Cassisi, S., Salaris, M., Anderson, J., et al. 2009, *ApJ*, 702, 1530
- Cassisi, S., Salaris, M., Pietrinferni, A., Vink, J. S., & Monelli, M. 2014, *A&A*, 571, A81
- Chantreau, W., Charbonnel, C., & Decressin, T. 2015, *A&A*, 578, A117
- Charbonnel, C., Chantreau, W., Decressin, T., Meynet, G., & Schaerer, D. 2013, *A&A*, 557, L17
- Córscico, A. H. & Althaus, L. G. 2006, *A&A*, 454, 863
- Córscico, A. H., Althaus, L. G., Benvenuto, O. G., & Serenelli, A. M. 2002, *A&A*, 387, 531
- Córscico, A. H., Althaus, L. G., Miller Bertolami, M. M., et al. 2012, *MNRAS*, 424, 2792
- D'Antona, F., Bellazzini, M., Caloi, V., et al. 2005, *ApJ*, 631, 868
- D'Antona, F. & Caloi, V. 2008, *MNRAS*, 390, 693
- D'Antona, F., Caloi, V., Montalbán, J., Ventura, P., & Gratton, R. 2002, *A&A*, 395, 69
- Decressin, T., Meynet, G., Charbonnel, C., Prantzos, N., & Ekström, S. 2007, *A&A*, 464, 1029
- Denissenkov, P. A. & Weiss, A. 2004, *ApJ*, 603, 119
- Ferguson, J. W., Alexander, D. R., Allard, F., et al. 2005, *ApJ*, 623, 585
- Fontaine, G. & Brassard, P. 2008, *PASP*, 120, 1043
- Fontaine, G., Brassard, P., & Bergeron, P. 2001, *PASP*, 113, 409
- García-Berro, E. & Oswalt, T. D. 2016, *New A Rev.*, 72, 1
- García-Berro, E., Torres, S., Althaus, L. G., et al. 2010, *Nature*, 465, 194
- Groenewegen, M. A. T., Sloan, G. C., Soszyński, I., & Petersen, E. A. 2009, *A&A*, 506, 1277
- Groenewegen, M. A. T., Whitelock, P. A., Smith, C. H., & Kerschbaum, F. 1998, *MNRAS*, 293, 18
- Hansen, B. M. S., Kalirai, J. S., Anderson, J., et al. 2013, *Nature*, 500, 51
- Iglesias, C. A. & Rogers, F. J. 1996, *ApJ*, 464, 943
- Imbriani, G., Costantini, H., Formicola, A., et al. 2005, *European Physical Journal A*, 25, 455
- Istrate, A. G., Tauris, T. M., Langer, N., & Antoniadis, J. 2014, *A&A*, 571, L3
- Jeffery, E. J., von Hippel, T., DeGennaro, S., et al. 2011, *ApJ*, 730, 35
- Joo, S.-J. & Lee, Y.-W. 2013, *ApJ*, 762, 36
- Magni, G. & Mazzitelli, I. 1979, *A&A*, 72, 134
- McDonald, I., van Loon, J. T., Decin, L., et al. 2009, *MNRAS*, 394, 831
- Miller Bertolami, M. M. 2016, *A&A*, 588, A25
- Miller Bertolami, M. M., Althaus, L. G., & García-Berro, E. 2013, *ApJ*, 775, L22
- Miller Bertolami, M. M., Althaus, L. G., Unglaub, K., & Weiss, A. 2008, *A&A*, 491, 253
- Miller Bertolami, M. M., Rohrmann, R. D., Granada, A., & Althaus, L. G. 2011, *ApJ*, 743, L33
- Milone, A. P. 2015, *MNRAS*, 446, 1672
- Milone, A. P., Marino, A. F., Cassisi, S., et al. 2012, *ApJ*, 754, L34
- Norris, J. E. 2004, *ApJ*, 612, L25
- Renedo, I., Althaus, L. G., Miller Bertolami, M. M., et al. 2010, *ApJ*, 717, 183
- Rohrmann, R. D., Althaus, L. G., García-Berro, E., Córscico, A. H., & Miller Bertolami, M. M. 2012, *A&A*, 546, A119
- Rosenfield, P., Marigo, P., Girardi, L., et al. 2014, *ApJ*, 790, 22
- Salaris, M., Althaus, L. G., & García-Berro, E. 2013, *A&A*, 555, A96
- Salaris, M. & Cassisi, S. 2005, *Evolution of Stars and Stellar Populations* (Hoboken (NJ): Wiley-VCH), 400
- Salaris, M., Serenelli, A., Weiss, A., & Miller Bertolami, M. 2009, *ApJ*, 692, 1013
- Schröder, K.-P. & Cuntz, M. 2005, *ApJ*, 630, L73
- Segretain, L., Chabrier, G., Hernanz, M., et al. 1994, *ApJ*, 434, 641
- Serenelli, A. M., Althaus, L. G., Rohrmann, R. D., & Benvenuto, O. G. 2002, *MNRAS*, 337, 1091
- Shingles, L. J., Doherty, C. L., Karakas, A. I., et al. 2015, *MNRAS*, 452, 2804
- Tailo, M., Di Criscienzo, M., D'Antona, F., Caloi, V., & Ventura, P. 2016, *MNRAS*, 457, 4525
- Tassoul, M., Fontaine, G., & Winget, D. E. 1990, *ApJS*, 72, 335
- Unno, W., Osaki, Y., Ando, H., Saio, H., & Shibahashi, H. 1989, *Nonradial oscillations of stars*, 2nd ed. (Tokyo: University of Tokyo Press)
- Vassiliadis, E. & Wood, P. R. 1993, *ApJ*, 413, 641
- Ventura, P., D'Antona, F., Mazzitelli, I., & Gratton, R. 2001, *ApJ*, 550, L65
- Wachlin, F. C., Miller Bertolami, M. M., & Althaus, L. G. 2011, *A&A*, 533, A139
- Weiss, A. & Ferguson, J. W. 2009, *A&A*, 508, 1343
- Winget, D. E. & Kepler, S. O. 2008, *ARA&A*, 46, 157
- Winget, D. E., Kepler, S. O., Campos, F., et al. 2009, *ApJ*, 693, L6

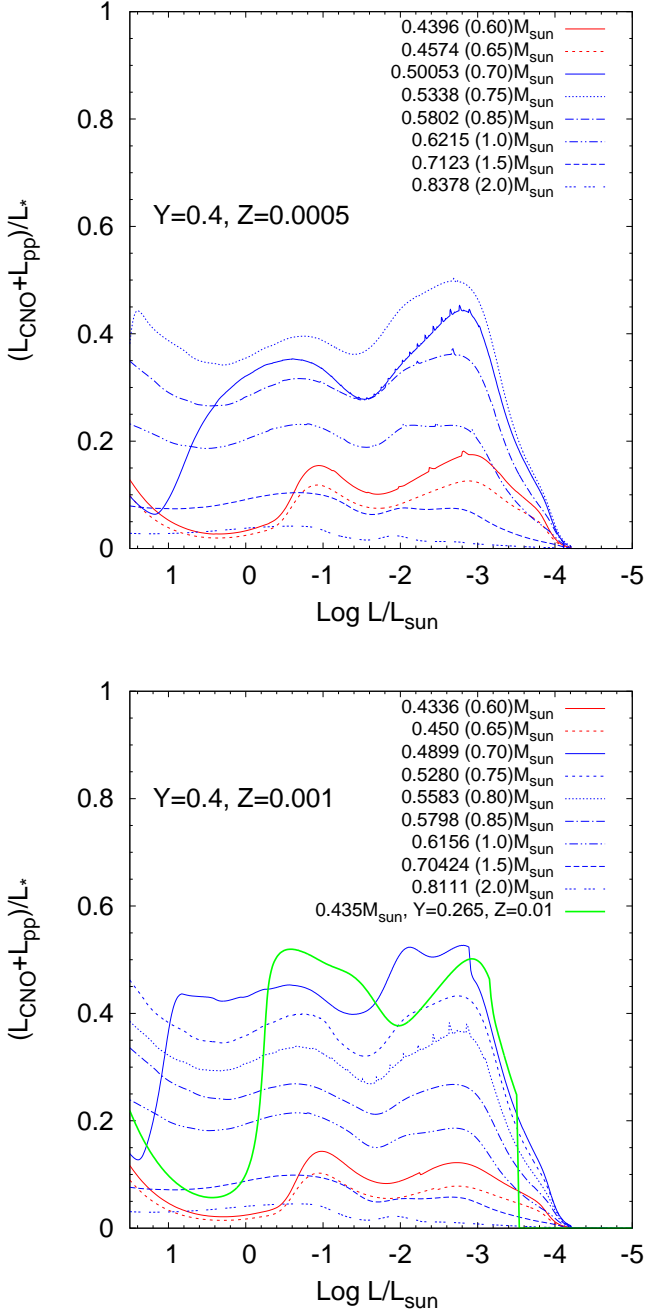


**Fig. 6.** Fraction of the total white dwarf luminosity due to hydrogen nuclear burning (CNO and  $pp$  burning) for all our helium-enhanced sequences for metallicity  $Z=0.0005$  and  $Z=0.001$  – upper and bottom panels, respectively – and initial helium mass fraction  $Y=0.4$ . Red (blue) lines show the predictions of our sequences that end as white dwarfs with helium (C/O) cores. The green line corresponds to a helium-core white dwarf sequence of  $0.435 M_{\odot}$  resulting from a progenitor with  $Z=0.01$  and standard initial helium abundance, taken from Althaus et al. (2013). Note that, for the less massive C/O white dwarfs, residual hydrogen burning becomes a relevant energy source even at low luminosities.

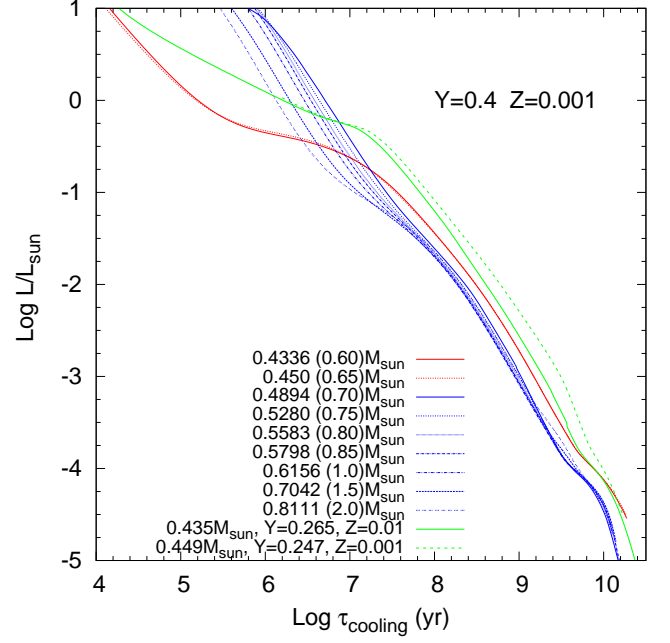


**Fig. 7.** Cooling times for all our helium-enhanced sequences with  $Z=0.001$  and initial helium mass fractions  $Y=0.4$ . Red and blue lines correspond, respectively, to white dwarfs with helium and C/O cores. The solid green line corresponds to a helium-core white dwarf of mass  $0.435 M_{\odot}$  resulting from a progenitor with  $Z=0.01$  and standard initial helium abundance (Althaus et al. 2013), whilst the dashed green line corresponds to helium-core white dwarfs of mass  $0.449 M_{\odot}$  resulting from a progenitor with  $Z=0.001$  and standard initial helium abundance (Serenelli et al. 2002).

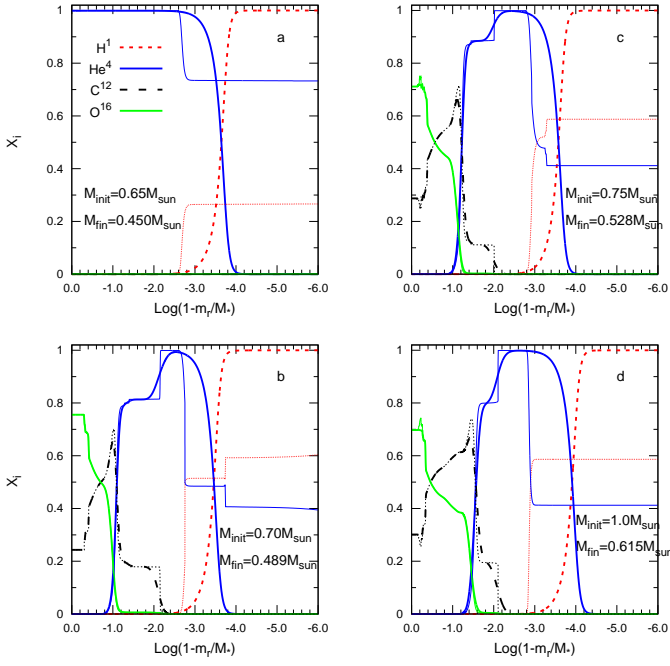


**Fig. 8.** Chemical abundance distribution of hydrogen, helium, carbon and oxygen in terms of the outer mass fraction for selected white dwarf models at the ZZ Ceti stage (thick lines) resulting from helium-enhanced progenitors with  $Z=0.001$  and initial helium abundance  $Y=0.4$ . The chemical profiles at the beginning of the cooling track are the thin lines. Panel a corresponds to a helium-core white dwarf resulting from a progenitor of initially  $M = 0.65 M_{\odot}$ , while panels b, c, and d to C/O white dwarfs resulting from progenitors with  $M = 0.70 M_{\odot}$ ,  $M = 0.75 M_{\odot}$ , and  $M = 1.0 M_{\odot}$ , respectively.

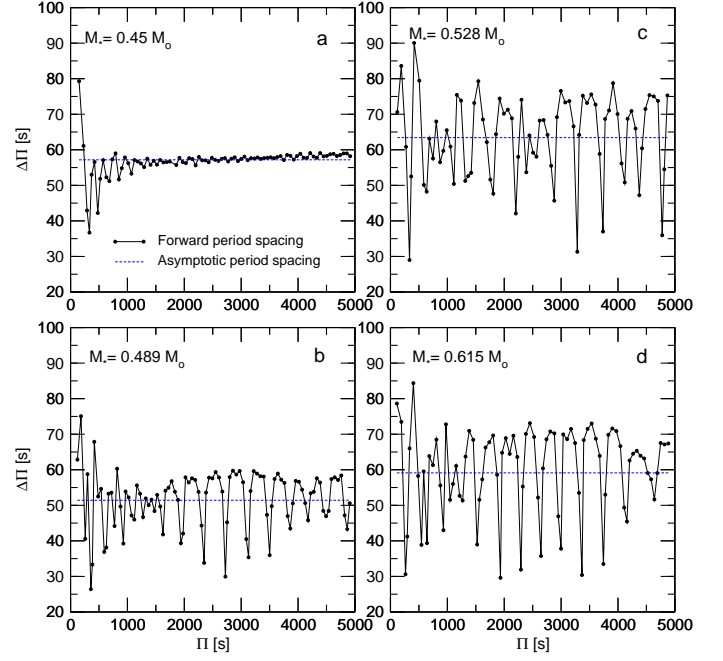


**Fig. 10.** The dipole ( $\ell = 1$ ) forward period spacing ( $\Delta P_{i_k}$ ) as a function of the periods ( $\Pi_k$ ) corresponding to the models shown in Fig. 8.

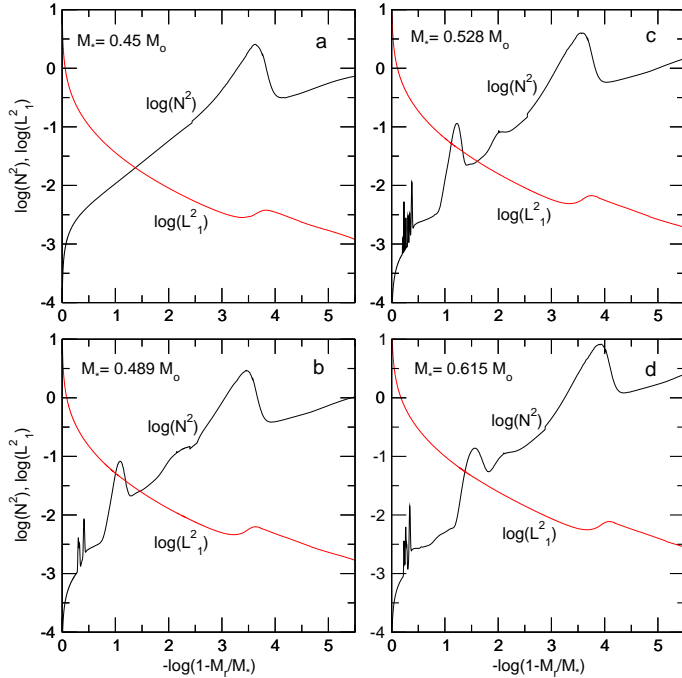


**Fig. 9.** Propagation diagrams – the spatial run of the logarithm of the squared Brunt-Väisälä and Lamb frequencies (Unno et al. 1989) – corresponding to the white dwarfs models shown in Fig. 8 for  $\ell = 1$ .